Impact-based probabilistic modeling of hydro-morphological processes in China (1985-2015)

Nan Wang[1,2], Weiming Cheng[2,3,4,5], Hongyan Zhang[1*], Cees van Westen[6], Junnan Xiong[2,7], Changjun Liu[8,9], Luigi Lombardo[6]

Abstract

Hydro-morphological processes (HMP, any natural phenomenon contained within the spectrum defined between debris flows and flash floods) pose a relevant threat to infrastructure, urban and rural settlements and to lives in general. This has been widely observed in recent years and will likely become worse as climate change will influence the spatio-temporal pattern of precipitation events. The modelling of where HMP-driven hazards may occur can help define the appropriate course of actions before and during a crisis, reducing the potential losses that HMPs cause in their wake. However, the probabilistic information on locations prone to experience a given hazard is not sufficient to depict the risk our society may incur. To cover this aspect, modeling the loss information could open up to better territorial management strategies.

In this work, we made use of the HMP catalogue of China. This catalogue reports reliable records from 1985 to 2015 across the whole Chinese territory. Specifically, we implemented the Light Gradient Boosting (LGB) classifier to model the impact level that locations across China have suffered from HMPs over the thirty-year record. In doing so, we estimated spatial probabilities of certain HMP impact, something that has yet to be tested in the natural hazard community, especially over such a large spatio-temporal domain.

This experiment follows a project launched by the Chinese government with the aim of improving national efforts against climate change and improving societal resilience to disastrous events. In this context, the good predictive performance our model produced suggest that the cartographic output could be useful to inform authorities of locations prone to human and infrastructural losses of specific magnitudes.

[1]Key Laboratory of Geographical Processes and Ecological Security in Changbai Mountains, Ministry of Education, School of Geographical Sciences, NortheastNormal University, Changchun, 130024, China

[2]State Key Laboratory of Resources and Environmental Information Systems, Institute of Geographic Sciences and Natural Resources Research, Chinese Academy of Sciences, Beijing, 100101, China

[3]University of Chinese Academy of Sciences, Beijing, 100049, China

[4]Jiangsu Center for Collaborative Innovation in Geographic Information Resource Development and Application, Nanjing, 210023, China

[5]Collaborative Innovation Center of South China Sea Studies, Nanjing, 210093, China

[6]University of Twente, Faculty of Geo-Information Science and Earth Observation (ITC), PO Box 217, Enschede, AE 7500, Netherlands

[7]School of Civil Engineering and Architecture, Southwest Petroleum University, Chengdu, 610500, China

[8]Research Center on Flood and Drought Disaster Reduction of the MWR, Beijing, 100038, China

[9]State Key Laboratory of Simulation and Regulation of Water Cycle in River Basin, China Institute of Water Resources and Hydropower Research, Beijing 100038, China

Keywords: Hydro-morphological processes; Hazard impact; Susceptibility modeling; China
Corresponding author: Hongyan Zhang
E-mail address: zhy@nenu.edu.cn

1 Introduction

Hydro-morphological processes (HMPs) define a spectrum of phenomena where a ill-defined proportion of water and solids can be mixed to produce debris flows, debris floods, or flash floods. These are particularly threatening natural hazards especially in mountainous landscapes. Their initiation and propagation can involve multiple catchments and their large capacity to cause damage is mainly due to our limited ability to respond to them once they take place. For instance, examples of flash floods exist with an observed concentration time of less than one hour (Iosub *et al.*, 2020). This implies that also our response time should be similar (Borga *et al.*, 2007; Hong *et al.*, 2013), which is why losses in terms of lives and infrastructure are not infrequent (Kobiyama and Goerl, 2007). Another aspect that makes HMPs particularly dangerous is our limited ability to predict them before they manifest. To estimate their genesis and behaviour, data-driven models are usually employed to define susceptible areas (Carrara *et al.*, 2008; Cama *et al.*, 2017) whereas physically-based models commonly solve runout simulations tasks (Pudasaini and Krautblatter, 2021; Van den Bout *et al.*, 2021). These two elements have been extensively researched and can currently rely on a number of models to produce reliable susceptibility and hazard estimates. In this overall context, a hazard magnitude scale has even been proposed to measure the severity of a given phenomenon (Wang and Sebastian, 2022). However, models that are able to quantify the potential impact of HMPs have been explored to a significantly lesser extent, with few valid exception (e.g., Diakakis *et al.*, 2020). This is likely due to the limited availability of complete databases listing the losses caused by natural hazards.

Recent studies indicate that society's awareness on HMPs largely depend on their impacts (de Bruijn *et al.*, 2019). Usually, disastrous events would capture the world's attention and thus leave a trace in all sorts of archives. Conversely, HMPs leading to limited losses might only be known by local communities, and might even be missed (Gaume *et al.*, 2009). These are the main reasons behind the incompleteness of HMP loss inventories. Some national scale exceptions do exist though. For instance, Switzerland has monitored HMP losses since 1972 and details on its national loss database can be found in Hilker *et al.* (2009); Andres and Badoux (2019). The US and Vietnam have also done the same, focusing exclusively on flooding though (see, Downton *et al.*, 2005; Luu *et al.*, 2019; Kreibich *et al.*, 2017). Turkey and Nepal have also developed their respective loss databases but centered around landslides and associated fatalities (Petley *et al.*, 2007; Görüm and Fidan, 2021). By examining these databases, one can infer that they often show an impact-frequency relation. In other words, the larger the loss the more infrequent its appearance in the database, and the smaller the loss the more analogous events are recorded. This is actually the idea behind risk assessment,

which boils down to understanding the frequency and impact relationship to derive quantities such as average annual loss, maximum probable loss and societal risk (Jaiswal *et al.*, 2011; Zielinski, 2017; Stroutn and McDougall, 2021).

Despite the obvious relevance, few cases exist where modeling societal risk is probabilistically sought in the context of natural hazards. Important contributions have paved the way in this direction and among them, Tsang *et al.* (2018) have proposed a risk function, albeit only in the context of earthquake losses. Rossi *et al.* (2019) have modeled the same, estimating the landslide societal risk for the whole Italian territory. Analogous researches have been carried out also for floods, with older examples from Italy (Salvati *et al.*, 2010) and the Netherlands (Jonkman *et al.*, 2011), and more recent ones from Portugal and Greece (Pereira *et al.*, 2017) as well as from the United Kingdom (Brown and Damery, 2002). Aside from the different level of complexity and site specific issues these articles deal with, one common element links them all together. In fact, most of the societal risk research is based on mortality data, leaving aside the economic aspect of the potential losses a given hazard may induce. These two elements are rarely combined under the overarching term "impact" and modeled accordingly (Tang *et al.*, 2021).

In this global overview, China has positioned itself with a number of studies based on specific test sites for landslides (Sui *et al.*, 2020), debris flows (Lan *et al.*, 2013) and floods (Li *et al.*, 2016). However, the need for a consistent HMP risk assessment at the national scale has long been discussed. With this idea in mind, few years ago China has launched an initiative to collect all HMP data from local administrations (location and date of occurrence) and whenever possible, also the associated losses (quantified both in terms of fatalities and economic damage), to be combined into a single digital database. This initiative has recently led to assess HMP occurrences in China over the last fifty years (Wang *et al.*, 2021a), explore their clustering behavior (Wang *et al.*, 2021c), derive HMP rainfall-thresholds (Wang *et al.*, 2021b) and produce the first national HMP space-time susceptibility model (Wang *et al.*, 2022a). These preliminary studies have therefore chiefly explored the occurrence information in the national database, leaving unexplored the loss one. Conversely, in this work we will attempt to make use of it, with the aim of creating a data-driven impact-based prediction model for the whole China.

The HMP Chinese database is mainly reliable from 1985, when China has welcomed the digital era revolutionizing the way administrations stored geographic data in Geographic Information Systems. And, it covers the period until 2015, when the HMP national database initiative was unfortunately terminated. In these thirty years of records, a total number of 24,898 is reported in the database, out of which 18,127 contained loss information. Therefore, we envisioned using this information to model the combined fatalities and economic losses with the aim of producing probabilities of HMP impact across the Chinese territory. In other words, we imagined a variation of the common susceptibility modeling framework, adapted here to different HMP impact levels. We recall here that the notion of susceptibility defines the probability of natural hazard occurrences on the basis of a set of predictors expressing

landscape and environmental characteristics (Reichenbach *et al.*, 2018). Over large areas, this is commonly achieved through binary classifiers belonging to the families of statistical (Lombardo and Mai, 2018) and/or machine/deep learning (Goetz *et al.*, 2015; Wang *et al.*, 2022b) models. By combining the loss information, it is possible to model the occurrence of events that have lead to different impact levels, each one being passed to a separate classifier. In turn, this produced the multi-impact prediction we present in this work.

The way we organized the manuscript includes a description of the data in Section 2; an overview of the modeling tools we used and the calibration and validation steps we followed in Section 3. The actual susceptibility is then presented in Section 4, which we interpret and discuss in Section 5. Ultimately, the conclusions are drawn in Section 6 to share our vision with the readers.

2 Data overview

The following sections will describe the HMP database and its characteristics, followed by an explanation of the mapping units of choice for this work and the predictor set we based our model on.

2.1 HMP inventory

The data we used in this study is extracted from the digital collection of Chinese HMP records (Liu *et al.*, 2018, 2021; Xiong *et al.*, 2019, 2020), each one characterized by geographic coordinates, time information and albeit partially, by a summary of sustained live and financial losses. From these records, we extracted all the HMPs for which a loss estimate was recorded between 1985 and 2015. The resulting subset accounted for 18,127 HMPs, whose loss records are graphically summarized in (Figure 1).

There, panel (a) shows the preprocessing step we introduced to account for the inflation in the considered period. The exchange rate we used is shown in panel (b). Thus, panel (a) essentially reports the inflation-adjusted values with respect to the US dollar (US$), which we used as a stable reference currency to compare the Chinese yuan (CNY) against. Panel (c) then depict the overall distribution of economic losses in log(USD) and panel (d) does the same for the number of HMP fatalities.

Several different factors can contribute to the HMPs' impact of their resulting damages to society (Špitalar *et al.*, 2014), but as a function of the losses they caused one may envision a rank system, from small to disastrous impacts. Following this reasoning, we classified the inventory into six categories combining fatalities and economic losses according to the informaiton provided in Table 1. There, Level M0 consist of a collection of records with minor losses and greater M-values imply an increase in the damage HMPs have generated. Specifically, the number of HMP records in each impact level are can be summarized as follows: 6,771 events associated to the M0 class, 8,616 to M1, 5,206 to M2, 2,257 to M3, 686 to M4, and 1,362 to M5. To provide a better context the spatial distribution of these events and

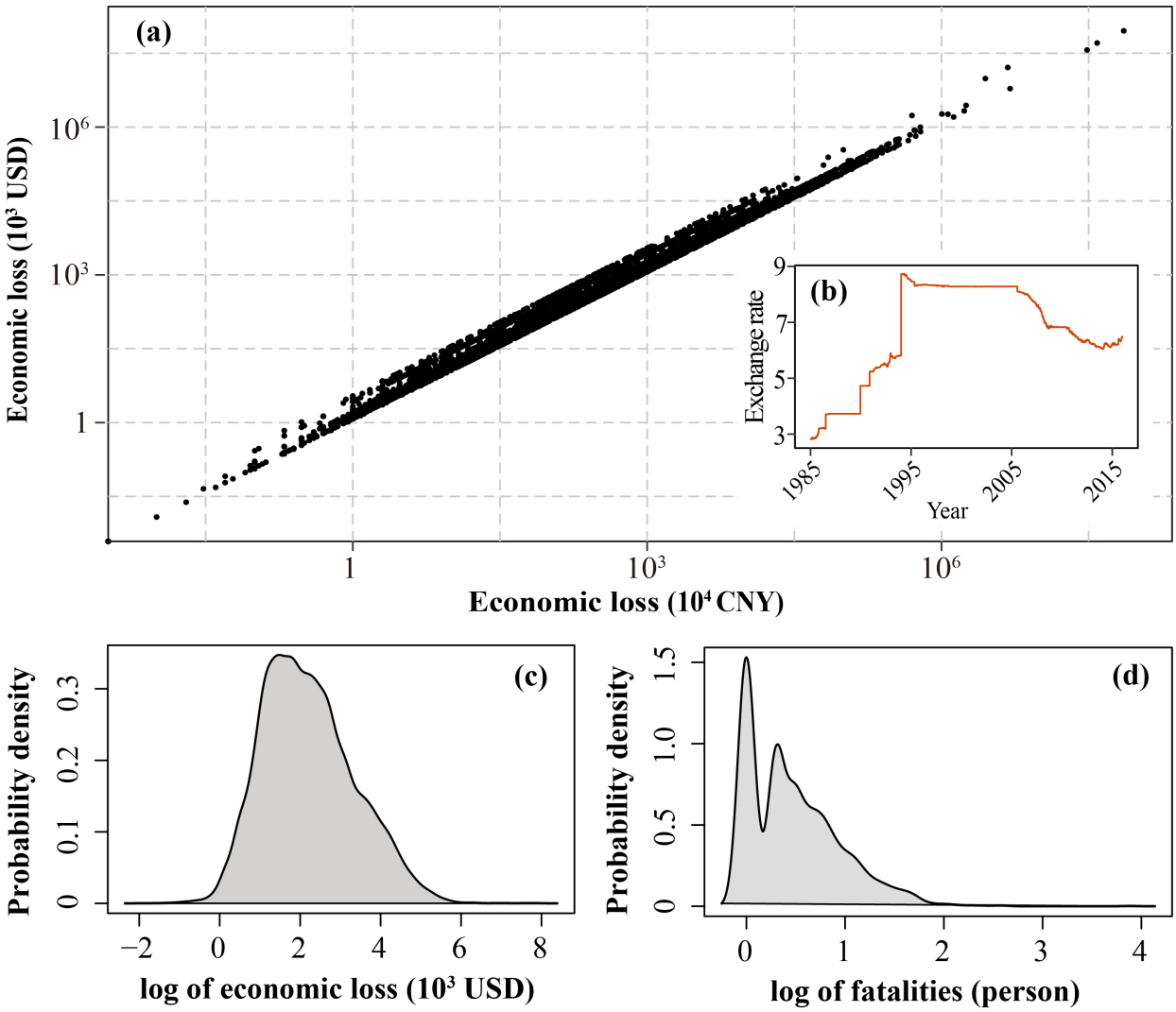

Figure 1: The time series of economic losses in Chinese RMB against the US dollars (a); The variation trend of the exchange rate between RMB and US dollars (b); Probability density distribution of fatalities (c) and economic losses (with inflation corrected) caused by HMPs across China during 1985-2015 (d).

relative impact classes, Figure 2 depicts this information across the whole Chinese territory, together with the current population density (LandScan, https://landscan.ornl.gov/).

Table 1: Impact classification criteria of HMPs.

Economic loss (thousand US $)	**Number of fatalities (person)**					
	0	**0-5**	**5-10**	**10-50**	**50-100**	**$\geq$ 100**
0	M0	M1	M2	M3	M4	M5
0-100	M1	M1	M2	M3	M4	M5
100-1,000	M2	M2	M2	M3	M4	M5
1,000-5,000	M3	M3	M3	M3	M4	M5
5,000-10,000	M4	M4	M4	M4	M4	M5
$\geq 10,000$	M5	M5	M5	M5	M5	M5

After the extraction of the HMPs and impact level information, we proceeded to assign a presence label to Chinese catchments (the mapping units we opted for in this study; see Section 2.2). For the catchments where multiple HMPs occurred across the 30-years record and specifically for the case where the impact level was different, we labeled the catchment with the highest impact level and disregarded the presence labeling for the lower impact. This operation ensured that impact classes would not suffer from autocorrelation issues and could thus be considered independent from each other. Overall, this lead the original number of HMPs to be aggregated at the catchment level, for which the number of positive samples in each model became 3,680 (M0), 4,348 (M1), 3,815 (M2), 2,026 (M3), 621 (M4), and 1,300 (M5). To create a balanced binary dataset, we randomly extracted an equal number of catchments without HMPs and labeled them with an absence case, for each impact class under consideration. The resulting 6 binary dataset will be the base for the subsequent modeling routine. The latter will feature the application of a machine-learning-based classifier (see Setion 3.1), equipped with an additional with Monte Carlo cross validation scheme aimed at informing on the prediction uncertainty (see Section 3.2).

2.2 Mapping units

Hydro-morphological processes including debris flows, debris floods, and flash floods, usually occur with various spatial extents. Due to the various physically-based processes, they can also be modeled at different scales and via different mapping units. Traditionally, examples exist where HMPs are modeled by utilizing a 10 to 1000m squared lattice. However, this kind of spatial partition cannot be used in our case because the size of the Chinese territory would result in billions of grid-cells or data points. Another reason for which we avoided

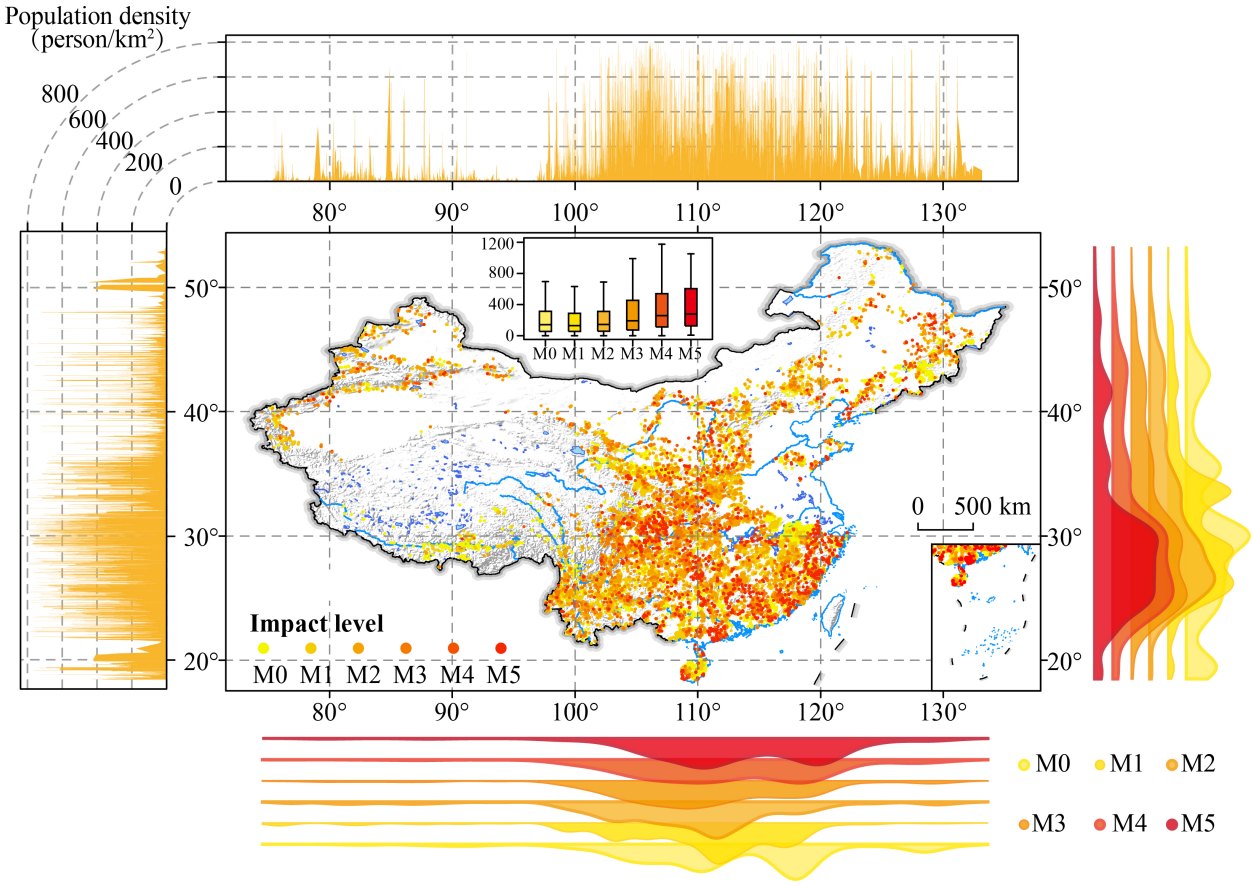

Figure 2: Geomorphological setting and distribution of HMPs with different impacts. The top and left plot show the variations of population density across longitude and latitude; the density plots presented in the bottom and right panels are the numbers of HMPs in each impact, and the boxplot in the middle of mapping shows the population density at each HMP spot within each impact.

using a mapping unit with a regular geometry has to do with the fact that terrain attributes and catchment characteristics are sensitive to the watershed boundary, which can be of vital importance for the HMPs. As a result, choosing a regular mapping unit large enough to produce a dataset small enough to be modeled would have been so large that the represetation of the catchment physiography would have been lost. Consequently, we have chosen to partition the Chinese territory into catchments, for they are ideal geographical, geomorphological and hydrological objects and also provide a computationally reasonable data size to work with. We accessed our mapping unit via the global watershed database HydroSHEDS (https://hydrosheds.org), which contains several levels to choose from. Among these, we selected the most detailed, corresponding to the 12^{th} level. In turn, this choice partitioned the whole Chinese territory into 73,587 catchments. The corresponding distribution of catchment sizes appears to be bimodal and spans from 0.1 km^2 to 667 km^2, with an average area of 130 km^2 and a 95% confidence interval of 231 km^2 (Figure 3).

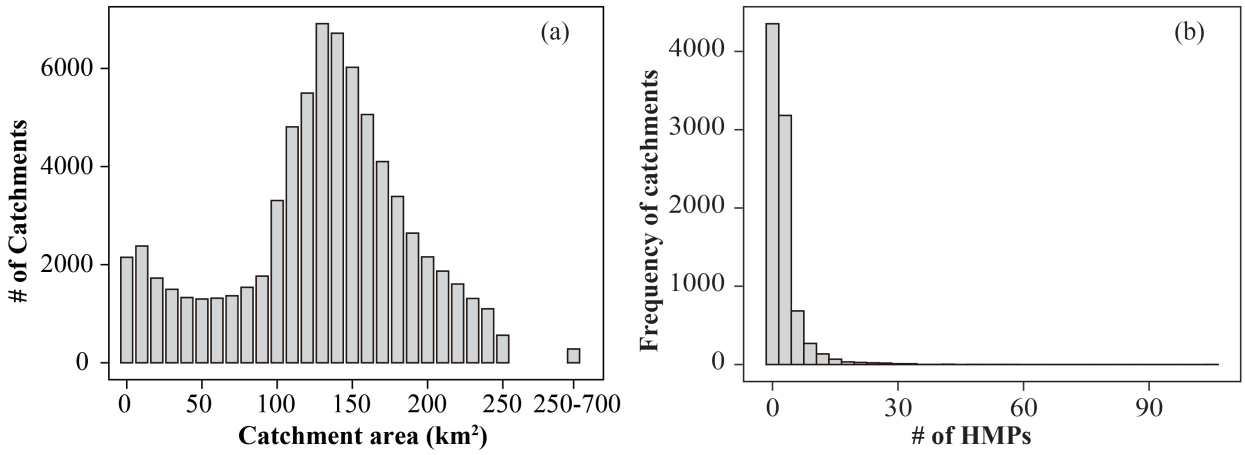

Figure 3: Distributions of catchment size (a) and HMPs count per catchment (b).

2.3 Explanatory variables

HMP susceptibility studies often list a number of explanatory variables or predictors, which mostly correspond to terrain, geological and pedological attributes, these being properties that can be considered time-invariant at the scale of our observation (Gariano and Guzzetti, 2016). Conversely, few cases features other environmental characteristics such as vegetation coverage, land use and precipitation, which otherwise exhibit significant variations within the considered time span (Lombardo *et al.*, 2020). Even if the model we propose here is purely spatial (details in Section 3), we considered a comprehensive predictor set, including static environmental characteristics as well as proxies for time-variant features within each catchment partitioning the Chinese territory.

Due to the coarse spatial extent that a catchment partition entails, the resolution of the predictors we chose leads to a distribution of potential values within each mapping unit. For

this reason, we then adopted the strategy of calculating mean and standard deviation values of each predictor distribution within each catchment. Notably, for those variables showing a marked temporal variation (e.g. daily rainfall, annual NDVI), we also computed mean and standard deviation values, though in this case we did so both in space and time (for the whole 30 years under consideration). This approach aims to capture the whole spatio-temporal predictor variability per catchment and its influence on HMPs and their induced losses.

Overall, we selected a total of 35 variables, 20 of which time-invariant and 15 time-variant ones. These featured terrain, stream system and catchment characteristics, soil type, climatic features, vegetation coverage, and human activities. A simpler overview of the predictors we considered is provided in **Appendix A**.

3 Methodology

We proposed to follow the classical strategy for model training and testing by splitting the samples into calibration and validation datasets. Here, we measured the predictive performance through the 5-fold cross validation scheme. The overall modeling protocol we implemented can be graphically summarized as follows (Figure 4):

3.1 Light Gradient Boosting

Gradient Boosting is a framework that uses a tree-based learning algorithm and has been applied widely in HMP susceptibility modelling (e.g. Lombardo *et al.*, 2015; Di *et al.*, 2019; Stanley *et al.*, 2020). Among a wide range of machine learning algorithms, Gradient Boosting has become the first choice of many researchers due to the good performance it ensures (Merghadi *et al.*, 2020). In our context, Gradient Boosting boils down to an ensemble of several decision trees (Friedman, 2001). The algorithm builds a model by iteratively and randomly building a decision tree as a weak classifier. Then, each decision tree is trained to approximate the negative gradient direction of the given loss function established in the previous iteration (i.e., the term of boosting). The strong classifier is eventually established by minimizing the loss function as much as possible without overfitting.

Light Gradient Boosting (LGB) is a novel kind of Gradient Boosting model (Merghadi *et al.*, 2020), which was proposed by Microsoft® in 2017 to develop a data-driven modeling routine capable of handling large amount of data. Specifically, LGB adopts a leaf-wise strategy when growing the decision tree, whereas Gradient Boosting is based on the level-wise growth strategy. Leaf-wise training is a more flexible way of working on "big data" while reducing the leaf loss and maintains the overall tree balance (Figure 5).

Notably, the optimal hyperparameter values we used are: $n\_estimators = 100$, $learning\_rate = 0.1$, $max\_depth = 30$, and $num\_leaves = 35$.

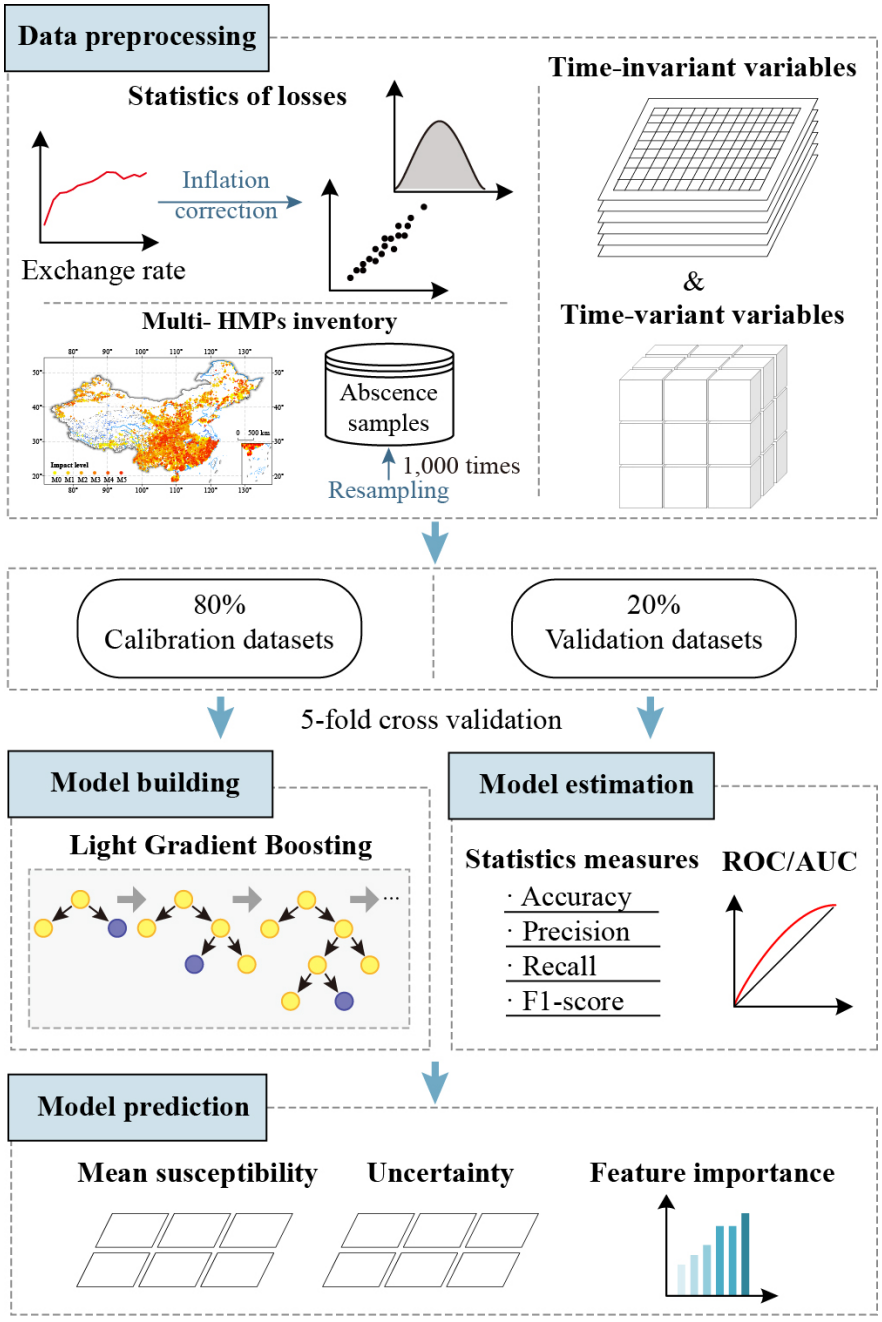

Figure 4: Flowchart of the methodology used in this study.

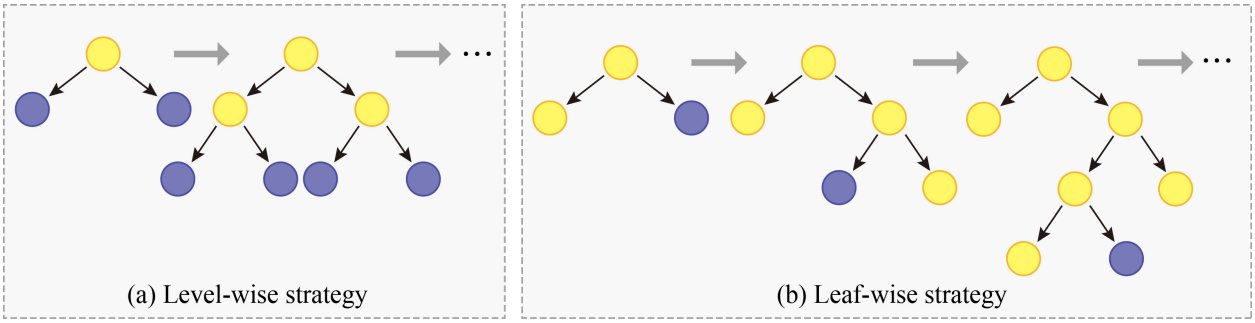

Figure 5: An illustration demonstrating the growing strategy between level-wise (a), and leaf-wise growth (b).

3.2 Uncertainty estimation

Here, we proposed to use the non-parametric Monte-Carlo simulation on the non-HMP datasets, which is implemented by utilizing 1,000 bootstrap replicates. We referred to this repeated sampling strategy proposed by Tang *et al.* (2019), and took advantage of the full information derived from the resampling procedure. Then, a large number of predictive models were built and used to obtain not only the mean value but also the uncertainty around it. The uncertainty analysis in this study were applied through the following steps:

1. Generate training datasets by sampling with replacement with the same number of positive samples from the negative ones. The iteration time is set to 1,000 for each training procedure.

2. Set several parameters to subset the samples and features for calibration model.

    - feature_fraction: 0.9, which indicates the portion for the feature selection when establishing a tree;
    - bagging_fraction: 0.8, which indicates the portion for subsamples when establishing a tree;
    - colsample_bytree: 0.8, which indicates the subsample ratio of columns when constructing each tree;
    - subsample: 0.8, which indicates the subset portion for the training.

3. Calculate the confidence interval (with 95% confidence level) for AUC values of each model by utilizing the difference between 97.5% and 2.5% percentiles from the whole bootstrapped realizations.

3.3 Model validation

The model evaluation is established on the basis of how the calibrated model can be used to generalize the prediction over unknown data. In this study, we considered cutoff dependent

and independent metrics to evaluate the performance of each bootstrapped model. Besides, the model robustness was obtained examining the relation between the width of the 95% CI and the mean susceptibility estimates, in a graphical summary referred to as error plot.

3.3.1 Cutoff dependent metrics

The most popular Cutoff dependent metrics measures for testing the prediction ability of a binary classification model include accuracy, precision, recall, and F1-score. These indices are calculated from the confusion matrix which describes the discrepancy between model predicted outcomes and the actual observed values. The combination of these metrics constitutes the suite we adopted in this study.

3.3.2 Cutoff independent metrics

Receiver Operating Characteristic curves (ROC) and the area under the curves (AUC) are another set of the most common tools for evaluating the performance of susceptibility models. ROC is consisted of x-axis setting as sensitivity (or recall, true positive rate, TPR) and y-axis indicating 1-specificity (or true negative rate, TNR). The performance of any classifier can then be evaluated on the basis of the AUC indications.

- Perfect performance: $AUC = 1$
- Outstanding performance: $0.8 < AUC < 0.9$
- Excellent performance: $0.7 < AUC < 0.8$
- Acceptable performance: $0.6 < AUC < 0.7$
- Poor performance: $0.5 < AUC < 0.6$

3.3.3 Error scatter plots

We use the error plot (i.e., the plot of the mean versus 95% CI of the probability spectrum) to evaluate whether the estimates oscillates with a trend that is acceptable for a classification task. In fact, a classifier should ideally return low and high probabilities associated with limited variation, whereas large differences are reasonably found in the middle portion of the probability distribution. The reasoning behind this assumption is for a user to trust whether the model classifies a presence or an absence with "confidence" (i.e., small width of the 95% CI), for additional references on this topic, see Rossi *et al.* (2010); Lombardo *et al.* (2020).

4 Results

4.1 Model performance

From the Monte-Carlo simulations, we obtained a thousand replicates of the susceptibility models and their relative performance metrics. Here, we provide a outlook by presenting the mean values out of the 1000 bootstraps, for each cutoff dependent indicator (see Table 2). WHat stands out is that our model is capable of recognizing M5 (Accuracy = 0.838, Precision = 0.818, Recall = 0.870, F1-score = 0.843) better than the other HMP impact classes. Overall, the accuracy is satisfying in all cases though, with values close to 0.8 and other metrics quite in line with the same model description. For instance, the HMP impact class our model struggles the most to classify among the six corresponds to M2, which is still associated with very good performance indicators far above 0.7. This in turn means that the LGB indeed returned suitable performance for each HMP class under consideration.

Table 2: The model performance on the validation datasets.

MOD	Accuracy	Precision	Recall	F1-score
M0	0.805	0.784	0.844	0.812
M1	0.800	0.777	0.842	0.808
M2	0.782	0.760	0.824	0.791
M3	0.798	0.770	0.849	0.808
M4	0.807	0.792	0.836	0.812
M5	0.838	0.818	0.870	0.843

Another insight on the LGB performance is provided in Figure 6. There the mean behavior can be examined in relation to the variability across the 1000 replicates. Specifically, we plotted the 1000 ROC curves (in grey) overimposing the mean one (in red). Then at the bottom of each panel, we reported the mean AUC value and its 95% CI (the difference between 2.5% and 97.5% of the AUC series). Interestingly, the performance are close to outstanding in all cases according to the evaluation scheme proposed by Hosmer and Lemeshow (2000). Interestingly, the M5 impact class is indeed the one LGB classifies better than the others but it is also worth noting that M3, M4 and M5 also exhibit a higher variability. This aspect can be further investigated via error plots, here shown in Figure 7.

The plots all show a bell-shaped trend which respects the assumption described in Section 3.3.3. Notably, for M0, M1 and M2, the uncertainties at the two extremes of the susceptibility distribution (along the x-axis) are mostly contained below a 0.5 width of the 95% CI. Mostly are actually concentrated below 0.25 (Figure 7a, Figure 7b, and 7c). The previous remark on the variability shown for M4 is also confirmed in this case with Figure 7e being

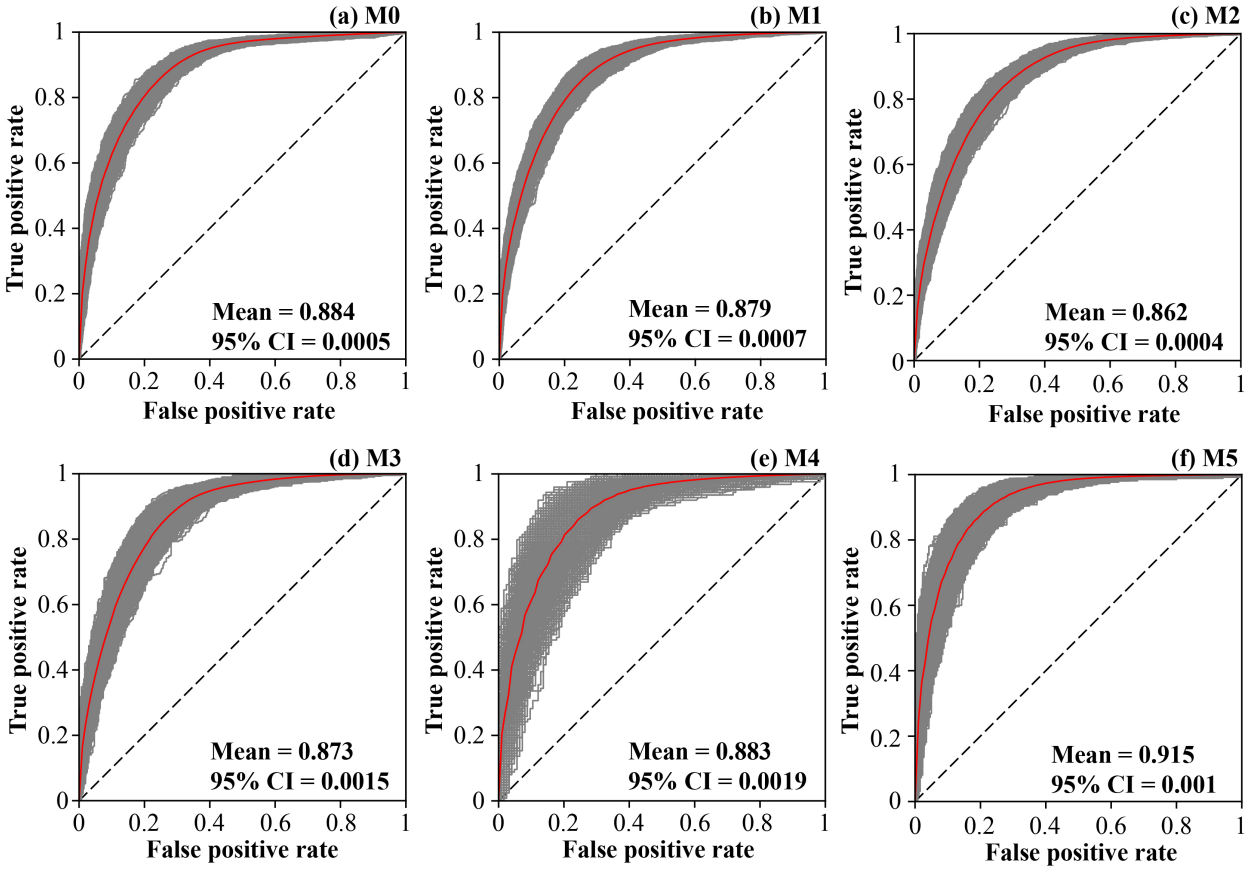

Figure 6: Goodness-of-fit summary of the impact-based susceptibility models.

shifted upward. As a result, the minimum value along the y-axis start close to 0.25. This means that a mean value of 0 could largely oscillate and looking at slightly larger values the variation around the mean could implicate probabilities reaching much higher picks in certain catchments. This is also, albeit to a lesser extent, the case for M5. This raises the question of where are these catchments located, so that one can at least note locations for which the model prediction is less robust. These geographical elements will be explored in Section 4.3.

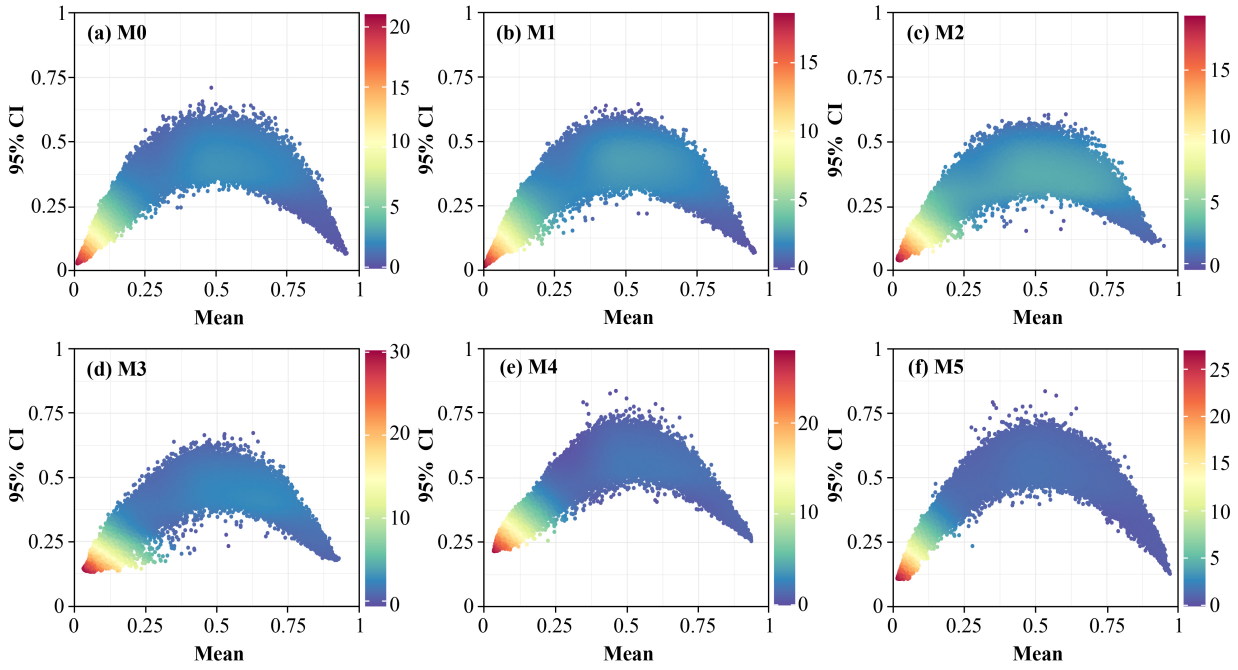

Figure 7: Error scatter plots for HMPs susceptibility detected via different models. Each point corresponds to a catchment.

4.2 Feature importance

To provide some elements of model interpretability, we explored the contribution of each predictor for each HMP impact class under consideration. The feature importance was calculated based on the mean predictors' contribution across the 1,000 resampling routines. For clarity, we only report the 10 highest contributors for each HMP impact class in Figure 8. There, the predictor importance highlights the role of the settlement areas. Intuitively, as we model losses caused by HMP, the presence of inhabitants and infrastructure is determining the level of impact one could expect. Besides, terrain features (e.g., ELV_μ, ELV_σ), stream/catchment features (e.g., Drainage density, Wandering ratio, Form factor), and vegetation coverage (e.g., $NDVI\_T_\mu\_S_\mu$, $NDVI\_T_\sigma\_S_\mu$), also largely explain the spatial distribution of each HMP impact class. Interestingly, climatic indices reveal a different contribution

with each impact class. For M5 and M3, among the climatic indices, the $RAIN\_T_A\_S_A$ contributes the most to the damage caused by HMPs. Conversely, $RAIN\_T_\sigma\_S_\mu$ plays a much more important role in M1 and M2, whereas $RAIN\_T_\mu\_S_\mu$ does the same for M4. This is likely due to the fact that being the six models built purely in space (the HMP losses do not vary in time), our attempt to capture the temporal effect of the predictors may be diluted to a certain degree considering the long time span we examined for their calculation.

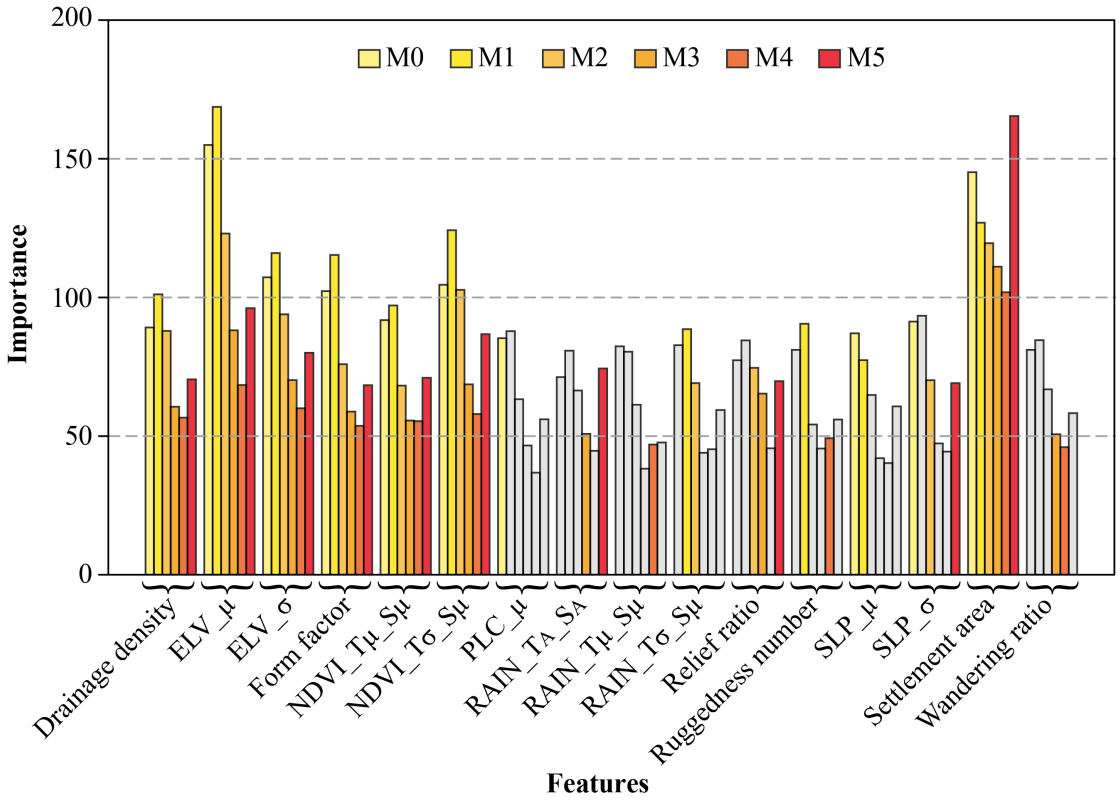

Figure 8: The top 10 features for each model. The grey bars indicate the variables rank out of 10 in the specific model.

4.3 Susceptibility mappings

The last step of any spatially-explicit model is to convert the prediction into map form. This was done both for the mean and 95% CI of the probabilities estimated for each of the six HMP impact classes. This is shown in Figure 9, where the spatial patterns of the two statistical moments appear to be similar and it is rather their relative amplitudes that mainly differentiate one impact class from the other. Overall, the areas that are more prone to exhibit losses belong to south-east China, whereas low probability values tend to show in China's north-westernmost sectors. Some marked differences can still be observed though. For instance, the most likely area to experience losses of a M1 level class is highlighted in the central part of China (Figure 9b). Conversely, the most likely areas to experience losses

in the scale of M4 and M5 are located in the south-east and along its coastlines (Figure 9e, f). As for M2 and M3, areas likely to be impacted at this levels span from south-east to central China (9c, d).

With regards to model uncertainties, we reclassified the 95% CI maps with a 0.1 percentile step, as shown in Figure 9 g-l. We can clearly see the relative variability in how likely the HMPs with a certain impact may occur across the Chinese territory. In most catchments that with a high susceptibility show a low uncertainty, which ensure the reliable decision on detecting the unstable catchments.

Due to the large area covered by China, it is difficult to appreciate the level at which the catchments' order we opted for partitions the whole landscape. For this reason, we selected three watersheds representative of various geomorphological settings and plotted the model results in Figure 10. These three catchments correspond to the Wu River (I), Tai Lake (II), and the 2^{nd} Songhua River (III), and they are all heavily affected by monsoons during spring and summer. Among them, watershed I is located in the Yungui Plateau and particularly in a region that severely suffers from soil erosion. This is most likely the reason why the HMP impact level associated with this sector is relatively high, because hydro-morphological phenomena can easily mobilize and transport large quantities of mixed material, increasing the damage potential of the flowing mass. Conversely, Watershed II lies in one of the most populated region belonging to the lower reaches of the Yangtze River. This may also explain the high HMP impact patches visible in the map, because the incoming mass may interact with particularly exposed and vulnerable communities. As for watershed III, this is located in the Changbai Mountains where the rainfall season is much shorter than the other two and the measured intensity is lower in comparison to catchment I and II. This may explain why the highest probability values of HMP impacts are less represented here for classes M1-M5 as compared to the other catchments.

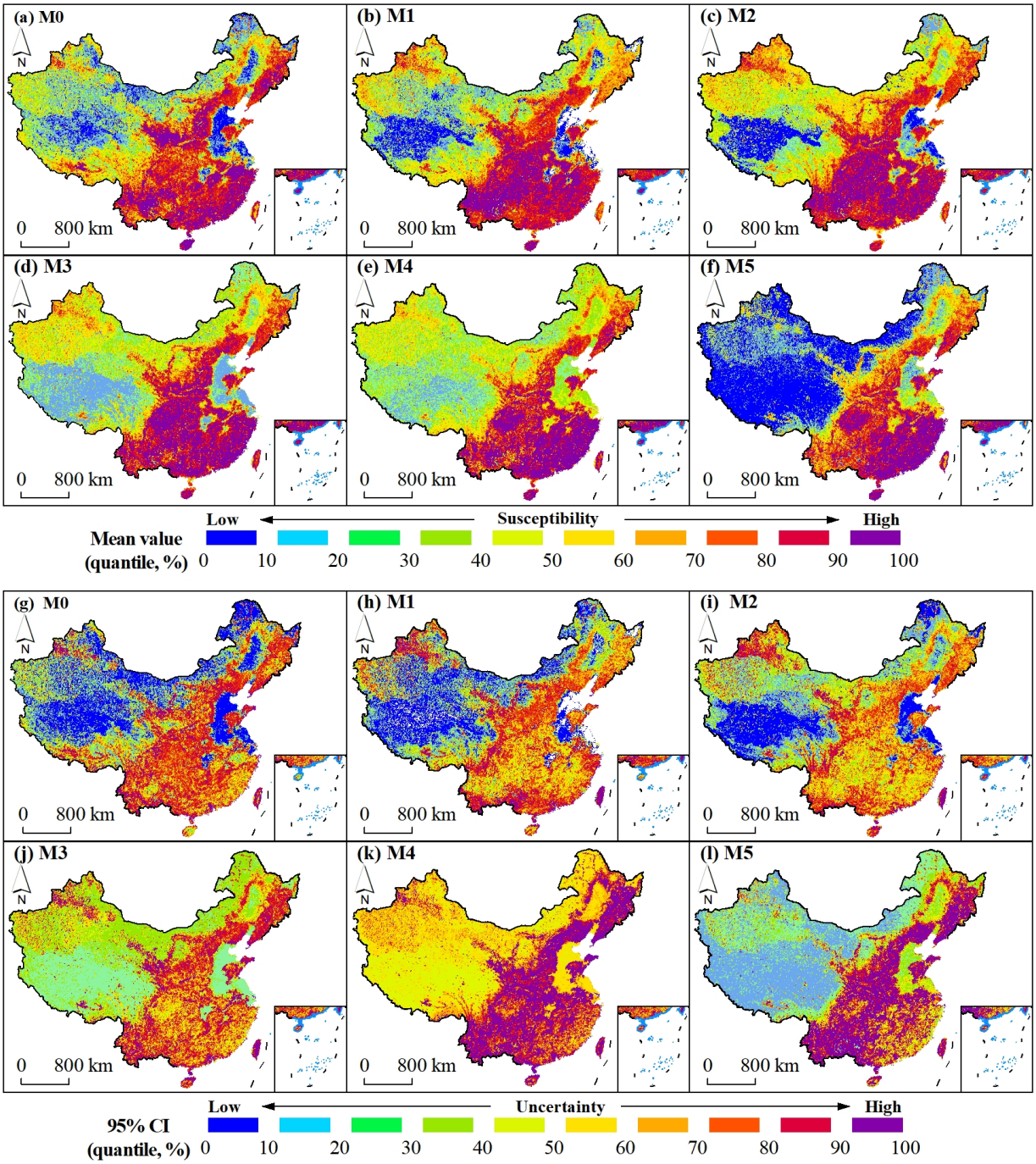

Figure 9: Mean susceptibility and uncertainty (measured with a 95% credible interval of the simulated susceptibilities) of HMPs with multi-impact in China during 1985-2015.

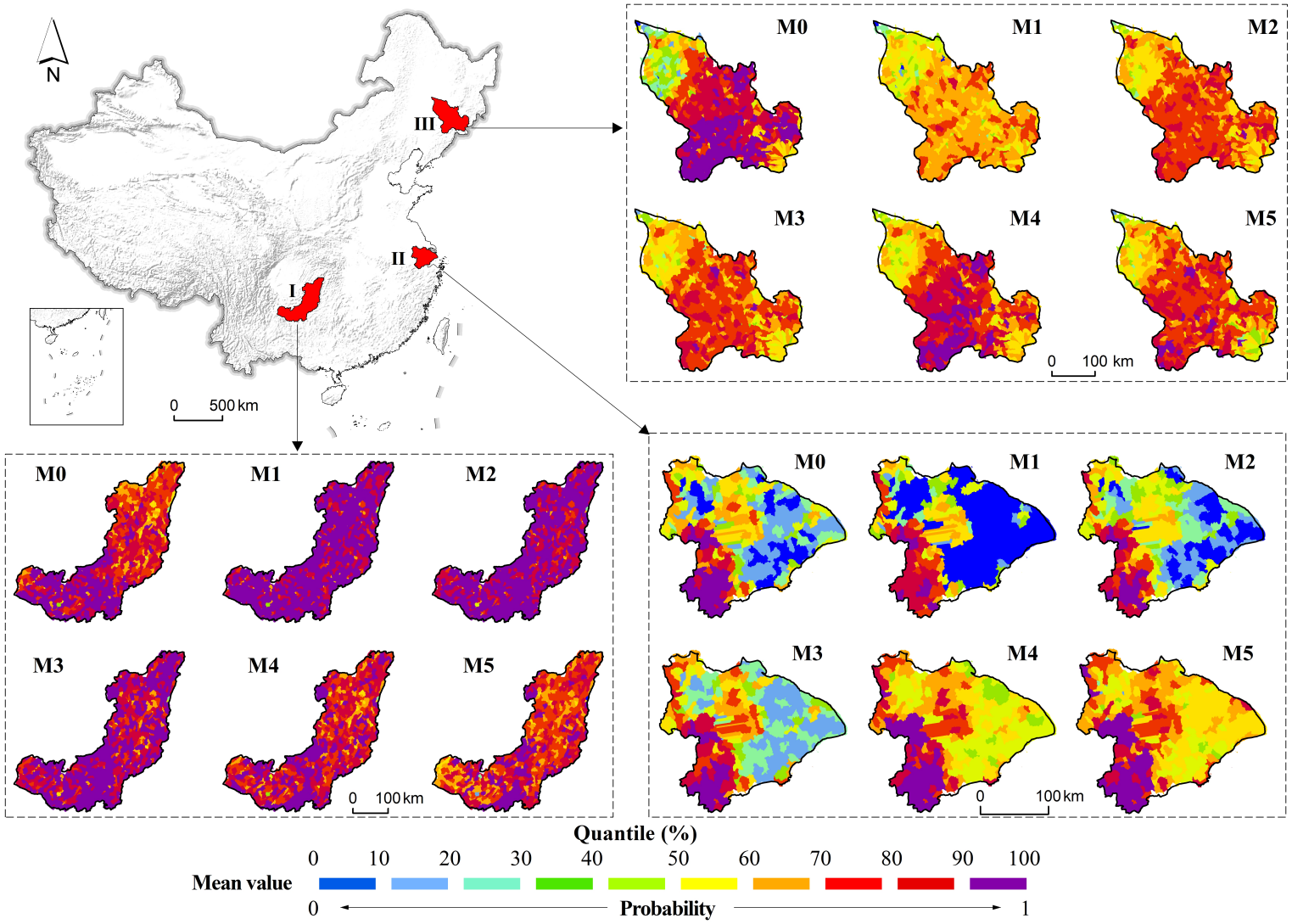

Figure 10: Mean susceptibility and uncertainty (measured with a 95% credible interval of the simulated susceptibilities) of HMPs with multi-impact in China during 1985-2015.

5 Discussions

Our findings emphasize a significant heterogeneity in the spatial probability of HMPs' occurrences. Looking at the bigger picture for the whole Chinese territory, this may not seem to hold validity across different HMP impact levels. However, a closer look at the level of major catchments opens up for a very different perspective, as our classifiers locally treat quite differently the probability of impact classes. For this reason, we opted to share the six model output as part of the supplementary material of this manuscript, to offer the same capacity to zoom in and out to any reader curious enough to visualize spatial patterns at different scales. Notably, these differences are consistent with the model contributions of the predictors we considered, because the use of separate classifiers lead to independent results. Examining the nuances among the different models, the spatial patterns they produces and interpreting their results was only possible because the Chinese database stored detailed loss information. This is something we would like to stress as one of the primary requirements to be included in standard natural hazards' inventories and catalogues. Unfortunately, this type of information is particularly scarce. Commonly, few analogous archives exist across the globe and when they do, their records tend to be severely biased. In fact, our society is naturally more prone to pay attention to greater losses and leave the smaller ones unattended or to the very least, to attend those with a lower level of consideration. This in turn means that our loss inventories may largely misrepresent the number of events where losses are of minor magnitude, although their frequency should be much higher than the extreme cases. And because of a natural higher frequency of small losses, their aggregated numbers could yield losses comparable to the few extreme cases, of which we tend to be more confident of. This is precisely the reason why in this work we opted to model not only the locations where extreme losses (M5 and M4) have been recorded, but we also opted to include medium (M3 and M2) and small (M1 and M0) ones. Our lucky starting point is that the mandate of the Chinese government was to store the loss information for all the events where an assessment, as minimal and local as it may have been, has been performed in the last thirty years.

Aside from the reflections dedicated to data completeness, we would like to stress that the spatial patterns we examined (and the predictor importance the model returned), point out at the fact that a combined effect of the anthropic fabric, together with climate and terrain characteristics constitute a sufficient level of information to explain the spatial variability of the HMP impacts. The spatial association of these elements, and particularly with respect to climate change are not new in relation to HMPs (e.g., Di *et al.*, 2019). However, what the scientific literature still lacks is the availability of a temporal dimension suitable to perform space-time models. In fact, as consistently recording losses is hardly performed, the numbers are often unsuitable to support statistical analyses. In our case, we started this work with the idea in mind of training a series of spatially-explicit models. But, we already envision a next step where the whole space-time domain is exploited to model HMP impact levels per Chinese catchments and opting this time for a yearly or even seasonal temporal partition of the thirty years under examination. Such a model should be able to shed more light

in the role of climate change with respect to HMP losses (Lin *et al.*, 2022), but also on how urban expansion correlates to them (Zhao *et al.*, 2022). Notably, China has undergone a large urbanization phase in the last few decades, which has certainly been associated with financial growth but also with an increased level of exposure to natural hazards. By looking at the spatial probabilities of HMP impact levels, M4 and M5 mostly affected densely urbanized/populated areas. These areas are predominant between latitudes 25° and 35° N, and longitudes 100° and 120° E, especially Sichuan basin, Yungui plateau, and the southeast coastal China. Particularly to the south, extreme precipitations have increasingly shifted towards higher intensities in recent years, something that may proportionally result in a greater risk in the region (Xiao *et al.*, 2018). For this reason, we stress the importance of research and actions directed on this topic and specifically for China, within the above mentioned southern sectors.

6 Conclusion

In this study, we determined the likelihood of Chinese catchments to suffer from HMP losses of six different magnitudes. The use of an artificially intelligent method such as the Light Gradient Boosting ensured high classification performance. However, we believe the most relevant aspect of this research resides in the combination of both economic losses and fatalities in a model able recognise and indicate areas where risk mitigation strategies should be considered by local authorities. In fact, the detail of the catchment partition we opted for is suitable to be integrated into local action plans. This being said, a number of extensions to the modeling framework we proposed here can already be envisioned. Extending the spatially-explicit nature of our model towards a space-time one could open up for near-real-time impact-based systems, an uncharted territory to be explored. These could be exploited as part of an exploratory assessment where link and dependencies between causes and effect can be holistically assessed. In a complementary manner and in the most wishful vision for the future, near-real-time impact-based systems could become operational tools though which providing impact-based forecast for communities to be informed on, for insurance companies to base their costs and for humanitarian organization to priorities their support.

Notably, to favor the dissemination of our work, we opted to share the model results in the supplementary materials (**Appendix B**), with the idea in mind of offering an interactive view of our output, which is otherwise a challenge in a traditional manuscript structure.

Acknowledgement

This work was supported by the National Natural Science Foundation of China (Grant No. 42201452), the Foundation of the Education Department of Jilin Province (Grant No. JJKH20211291KJ), and the China Postdoctoral Science Foundation (Grant No. 2022T150057). We also thank for the support of China National Flash Flood Disasters Pre-

vention and Control Project from the China Institute of Water Resources and Hydropower Research (IWHR).

Appendix A. Summary of the covariate set

- **Terrain features**

  1. ELV_μ: Mean of Elevation
  2. ELV_σ: Standard deviation of Elevation
  3. SLP_μ: Mean of Slope Steepness
  4. SLP_σ: Standard deviation of Slope Steepness
  5. PLC_μ: Mean of Plan Curvature
  6. PLC_σ: Standard deviation of Plan Curvature
  7. PRC_μ: Mean of Profile Curvature
  8. PRC_σ: Standard deviation of Profile Curvature

- **Stream/Catchment features**

  1. Wandering ratio (Chorley, 1957): $R_W = \frac{L_{MF}}{L_B}$
  2. Fitness ratio (Melton, 1957): $R_f = \frac{L_{MF}}{P}$
  3. Form factor (Horton, 1932): $F_f = \frac{A}{L_B}$
  4. Circularity ratio (Miller and Summerson, 1960): $R_c = \frac{4\pi A}{P^2}$
  5. Elongation ratio (Schumm, 1956): $R_e = \frac{2}{L_B \times (A/\pi)^{0.5}}$
  6. Relief ratio (Schumm, 1956): $R_r = \frac{R_B}{L_B}$
  7. Compactness coefficient (Gravelius, 1914):$C_c = 0.2841 \frac{P}{A^{0.5}}$
  8. Drainage density (Strahler, 1952): $D_d = \frac{L_v}{A}$
  9. Ruggedness number (Strahler, 1958): $R_n = R_B \times D_d$
  10. Lemniscate's value (Chorley, 1957): $k = \frac{L_B^2}{A}$

- **Soil type**
  This parameter is expressed as the area percentage of each soil type per catchment and includes: Clay, Clay Loam, Loam, Loamy Sand, Sand, Sandy Clay, Sandy Clayey Loam, Sandy Loam, Silt, Silty Clay, Silty Clayey Loam, and Silty Loam.

- **Climatic zone**
  This parameter is expressed ad the area percentage of climatic zone per catchment and includes: North Temperate, Central Temperate, South Temperate, North Subtropic, Central Subtropic, South Subtropic, North Tropic, Central Tropic, Highland.

- **Climatic indices**

  1. $RAIN\_T_{\mu}\_S_{\mu}$: The temporal mean estimated from the daily rainfall for each year (T_{μ}) spatially aggregated ad the mean computed for the whole catchment (S_{μ}).
  2. $RAIN\_T_{\mu}\_S_{\sigma}$: The temporal mean estimated from the daily rainfall for each year (T_{μ}) spatially aggregated as the standard deviation computed for the whole catchment (S_{σ}).
  3. $RAIN\_T_{\sigma}\_S_{\mu}$: The temporal standard deviation estimated from the daily rainfall for each year (T_{σ}) spatially aggregated as the mean computed for the whole catchment (S_{μ}).
  4. $RAIN\_T_{\sigma}\_S_{\sigma}$: The temporal standard deviation estimated from the daily rainfall for each year (T_{σ}) spatially aggregated as the standard deviation computed for the whole catchment (S_{σ}).
  5. $AnnualRAIN\_S_{\mu}$: The mean annual rainfall for each year spatially aggregated as mean for the whole catchment (S_{μ}).
  6. $AnnualRAIN\_S_{\sigma}$: The mean annual rainfall for each year spatially aggregated as standard deviation for the whole catchment (S_{σ}).
  7. $RAIN\_T_{A}\_S_{A}$: The maximum daily rainfall for each year (T_A) spatially aggregated as maximum computed for the whole catchment (S_A).
  8. $RAIN\_T_{A}\_S_{\mu}$: The maximum daily rainfall for each year (T_A) spatially aggregated as mean computed for the whole catchment (S_{μ}).

- **NDVI**

  1. $NDVI\_T_{\mu}\_S_{\mu}$: The temporal mean estimated from each NDVI acquisition for each year (T_{μ}) spatially aggregated as the mean computed for the whole catchment (S_{μ}).
  2. $NDVI\_T_{\mu}\_S_{\sigma}$: The temporal mean estimated from each NDVI acquisition for each year (T_{μ}) spatially aggregated as the standard deviation computed for the whole catchment (S_{σ}).
  3. $NDVI\_T_{\sigma}\_S_{\mu}$: The temporal standard deviation estimated from each NDVI acquisition for each year (T_{σ}) spatially aggregated as the mean computed for the whole catchment (S_{μ}).
  4. $NDVI\_T_{\sigma}\_S_{\sigma}$: The temporal standard deviation estimated from each NDVI acquisition for each year (T_{σ}) spatially aggregated as the standard deviation computed for the whole catchment (S_{σ}).

- **Settlement area**

  The estimated settlement area per polygon expressed in km^2 for each year.

- **Land use**
  The land use type in each catchment. This is a category variable.

- **Antecedent HMPs**
  The cumulative number of HMPs occurred in a three-year time window before each considered year.

Appendix B. Supplementary data

References

Andres, N. and Badoux, A. (2019) The Swiss flood and landslide damage database: normalisation and trends. *Journal of Flood Risk Management* **12**, e12510.

Borga, M., Boscolo, P., Zanon, F. and Sangati, M. (2007) Hydrometeorological analysis of the 29 August 2003 flash flood in the Eastern Italian Alps. *Journal of Hydrometeorology* **8**(5), 1049–1067.

Van den Bout, B., Lombardo, L., Chiyang, M., van Westen, C. and Jetten, V. (2021) Physically-based catchment-scale prediction of slope failure volume and geometry. *Engineering Geology* **284**, 105942.

Brown, J. D. and Damery, S. L. (2002) Managing flood risk in the UK: towards an integration of social and technical perspectives. *Transactions of the Institute of British Geographers* **27**(4), 412–426.

de Bruijn, J. A., de Moel, H., Jongman, B., de Ruiter, M. C., Wagemaker, J. and Aerts, J. C. (2019) A global database of historic and real-time flood events based on social media. *Scientific Data* **6**(1), 1–12.

Cama, M., Lombardo, L., Conoscenti, C. and Rotigliano, E. (2017) Improving transferability strategies for debris flow susceptibility assessment: Application to the Saponara and Itala catchments (Messina, Italy). *Geomorphology* **288**, 52–65.

Carrara, A., Crosta, G. and Frattini, P. (2008) Comparing models of debris-flow susceptibility in the alpine environment. *Geomorphology* **94**(3-4), 353–378.

Chorley, R. J. (1957) Illustrating the laws of morphometry. *Geological Magazine* **94**(2), 140–150.

Di, B., Zhang, H., Liu, Y., Li, J., Chen, N., Stamatopoulos, C. A., Luo, Y. and Zhan, Y. (2019) Assessing susceptibility of debris flow in southwest China using gradient boosting machine. *Scientific Reports* **9**(1), 1–12.

Diakakis, M., Deligiannakis, G., Antoniadis, Z., Melaki, M., Katsetsiadou, N., Andreadakis, E., Spyrou, N. and Gogou, M. (2020) Proposal of a flash flood impact severity scale for the classification and mapping of flash flood impacts. *Journal of Hydrology* p. 125452.

Downton, M. W., Miller, J. Z. B. and Pielke Jr, R. A. (2005) Reanalysis of US National Weather Service flood loss database. *Natural Hazards Review* **6**(1), 13–22.

Friedman, J. H. (2001) Greedy function approximation: a gradient boosting machine. *Annals of Statistics* pp. 1189–1232.

539 Gariano, S. L. and Guzzetti, F. (2016) Landslides in a changing climate. *Earth-Science*
540 *Reviews* **162**, 227–252.

541 Gaume, E., Bain, V., Bernardara, P., Newinger, O., Barbuc, M., Bateman, A., Blaškovičová,
542 L., Blöschl, G., Borga, M., Dumitrescu, A. *et al.* (2009) A compilation of data on European
543 flash floods. *Journal of Hydrology* **367**(1-2), 70–78.

544 Goetz, J., Brenning, A., Petschko, H. and Leopold, P. (2015) Evaluating machine learning
545 and statistical prediction techniques for landslide susceptibility modeling. *Computers &*
546 *Geosciences* **81**, 1–11.

547 Görüm, T. and Fidan, S. (2021) Spatiotemporal variations of fatal landslides in Turkey.
548 *Landslides* **18**(5), 1691–1705.

549 Gravelius, H. (1914) Flusskunde. Goschen Verlagshan dlug Berlin. En Zavoianu, I. 1985.
550 *Morphometry of drainage basins. Elsevier, Amsterdam* .

551 Hilker, N., Badoux, A. and Hegg, C. (2009) The Swiss flood and landslide damage database
552 1972–2007. *Natural Hazards and Earth System Sciences* **9**(3), 913–925.

553 Hong, Y., Adhikari, P. and Gourley, J. J. (2013) Flash flood.

554 Horton, R. E. (1932) Drainage-basin characteristics. *Eos, Transactions American Geophys-*
555 *ical Union* **13**(1), 350–361.

556 Hosmer, D. W. and Lemeshow, S. (2000) *Applied Logistic Regression*. Second edition. New
557 York: Wiley.

558 Iosub, M., Minea, I., Chelariu, O. E. and Ursu, A. (2020) Assessment of flash flood suscepti-
559 bility potential in Moldavian Plain (Romania). *Journal of Flood Risk Management* **13**(4),
560 e12588.

561 Jaiswal, P., Van Westen, C. and Jetten, V. (2011) Quantitative estimation of landslide risk
562 from rapid debris slides on natural slopes in the Nilgiri hills, India. *Natural Hazards and*
563 *Earth System Sciences* **11**(6), 1723–1743.

564 Jonkman, S. N., Jongejan, R. and Maaskant, B. (2011) The use of individual and societal
565 risk criteria within the Dutch flood safety policy—Nationwide estimates of societal risk
566 and policy applications. *Risk Analysis: An International Journal* **31**(2), 282–300.

567 Kobiyama, M. and Goerl, R. F. (2007) Quantitative method to distinguish flood and flash
568 flood as disasters. *SUISUI Hydrological Research Letters* **1**, 11–14.

569 Kreibich, H., Thieken, A., Haubrock, S.-N. and Schröter, K. (2017) HOWAS21, the German
570 flood damage database. *Flood Damage Survey and Assessment* pp. 65–75.

Lan, H., Li, L., Zhang, Y., Gao, X. and Liu, H. (2013) Risk assessment of debris flow in Yushu seismic area in China: a perspective for the reconstruction. *Natural Hazards and Earth System Sciences* **13**(11), 2957–2968.

Li, C., Cheng, X., Li, N., Du, X., Yu, Q. and Kan, G. (2016) A framework for flood risk analysis and benefit assessment of flood control measures in urban areas. *International Journal of Environmental Research and Public Health* **13**(8), 787.

Lin, Q., Steger, S., Pittore, M., Zhang, J., Wang, L., Jiang, T. and Wang, Y. (2022) Evaluation of potential changes in landslide susceptibility and landslide occurrence frequency in China under climate change. *Science of the Total Environment* **850**, 158049.

Liu, Y., Huang, Y., Wan, J., Yang, Z. and Zhang, X. (2021) Analysis of human activity impact on flash floods in China from 1950 to 2015. *Sustainability* **13**(1), 217.

Liu, Y., Yang, Z., Huang, Y. and Liu, C. (2018) Spatiotemporal evolution and driving factors of China's flash flood disasters since 1949. *Science China Earth Sciences* **61**(12), 1804–1817.

Lombardo, L., Cama, M., Conoscenti, C., Märker, M. and Rotigliano, E. (2015) Binary logistic regression versus stochastic gradient boosted decision trees in assessing landslide susceptibility for multiple-occurring landslide events: application to the 2009 storm event in Messina (Sicily, southern Italy). *Natural Hazards* **79**(3), 1621–1648.

Lombardo, L. and Mai, P. M. (2018) Presenting logistic regression-based landslide susceptibility results. *Engineering Geology* **244**, 14–24.

Lombardo, L., Opitz, T., Ardizzone, F., Guzzetti, F. and Huser, R. (2020) Space-time landslide predictive modelling. *Earth-Science Reviews* p. 103318.

Luu, C., von Meding, J. and Mojtahedi, M. (2019) Analyzing Vietnam's national disaster loss database for flood risk assessment using multiple linear regression-TOPSIS. *International Journal of Disaster Risk Reduction* **40**, 101153.

Melton, M. A. (1957) An analysis of the relations among elements of climate, surface properties, and geomorphology. Technical report, Columbia Univ New York.

Merghadi, A., Yunus, A. P., Dou, J., Whiteley, J., ThaiPham, B., Bui, D. T., Avtar, R. and Abderrahmane, B. (2020) Machine learning methods for landslide susceptibility studies: A comparative overview of algorithm performance. *Earth-Science Reviews* p. 103225.

Miller, O. and Summerson, C. H. (1960) Slope-zone maps. *Geographical review* **50**(2), 194–202.

Pereira, S., Diakakis, M., Deligiannakis, G. and Zêzere, J. (2017) Comparing flood mortality in Portugal and Greece (Western and eastern Mediterranean). *International Journal of Disaster Risk Reduction* **22**, 147–157.

Petley, D. N., Hearn, G. J., Hart, A., Rosser, N. J., Dunning, S. A., Oven, K. and Mitchell, W. A. (2007) Trends in landslide occurrence in Nepal. *Natural Hazards* **43**(1), 23–44.

Pudasaini, S. P. and Krautblatter, M. (2021) The mechanics of landslide mobility with erosion. *Nature Communications* **12**(1), 1–15.

Reichenbach, P., Rossi, M., Malamud, B. D., Mihir, M. and Guzzetti, F. (2018) A review of statistically-based landslide susceptibility models. *Earth-Science Reviews* **180**, 60–91.

Rossi, M., Guzzetti, F., Reichenbach, P., Mondini, A. C. and Peruccacci, S. (2010) Optimal landslide susceptibility zonation based on multiple forecasts. *Geomorphology* **114**(3), 129–142.

Rossi, M., Guzzetti, F., Salvati, P., Donnini, M., Napolitano, E. and Bianchi, C. (2019) A predictive model of societal landslide risk in Italy. *Earth-Science Reviews* **196**, 102849.

Salvati, P., Bianchi, C., Rossi, M. and Guzzetti, F. (2010) Societal landslide and flood risk in Italy. *Natural Hazards and Earth System Sciences* **10**(3), 465–483.

Schumm, S. A. (1956) Evolution of drainage systems and slopes in badlands at Perth Amboy, New Jersey. *Geological Society of America bulletin* **67**(5), 597–646.

Špitalar, M., Gourley, J. J., Lutoff, C., Kirstetter, P.-E., Brilly, M. and Carr, N. (2014) Analysis of flash flood parameters and human impacts in the US from 2006 to 2012. *Journal of Hydrology* **519**, 863–870.

Stanley, T., Kirschbaum, D., Sobieszczyk, S., Jasinski, M., Borak, J. and Slaughter, S. (2020) Building a landslide hazard indicator with machine learning and land surface models. *Environmental Modelling & Software* **129**, 104692.

Strahler, A. N. (1952) Hypsometric (area-altitude) analysis of erosional topography. *Geological Society of America Bulletin* **63**(11), 1117–1142.

Strahler, A. N. (1958) Dimensional analysis applied to fluvially eroded landforms. *Geological Society of America Bulletin* **69**(3), 279–300.

Strouth, A. and McDougall, S. (2021) Societal risk evaluation for landslides: historical synthesis and proposed tools. *Landslides* **18**(3), 1071–1085.

Sui, H., Hu, R., Gao, W., Gao, W. and Luo, G. (2020) Risk assessment of individual landslide based on the risk acceptable model: a case study of the Shiyantan landslide in Mayang County, China. *Human and Ecological Risk Assessment: An International Journal* **26**(9), 2500–2519.

Tang, J., Li, W., Fang, J., Zhang, Z., Du, S., Wu, Y. and Wen, J. (2021) Scenario-based economic and societal risk assessment of storm flooding in Shanghai. *International Journal of Climate Change Strategies and Management* **13**(4/5), 529–546.

Tang, X., Hong, H., Shu, Y., Tang, H., Li, J. and Liu, W. (2019) Urban waterlogging susceptibility assessment based on a PSO-SVM method using a novel repeatedly random sampling idea to select negative samples. *Journal of Hydrology* **576**, 583–595.

Tsang, H.-H., Daniell, J. E., Wenzel, F. and Werner, A. C. (2018) A semi-probabilistic procedure for developing societal risk function. *Natural Hazards* **92**(2), 943–969.

Wang, N., Cheng, W., Lombardo, L., Xiong, J. and Guo, L. (2021a) Statistical spatiotemporal analysis of hydro-morphological processes in China during 1950–2015. *Stochastic Environmental Research and Risk Assessment* pp. 1–21.

Wang, N., Cheng, W., Marconcini, M., Bachofer, F., Liu, C., Xiong, J. and Lombardo, L. (2022a) Space-time susceptibility modeling of hydro-morphological processes at the Chinese national scale. *Engineering Geology* **301**, 106586.

Wang, N., Lombardo, L., Gariano, S. L., Cheng, W., Liu, C., Xiong, J. and Wang, R. (2021b) Using satellite rainfall products to assess the triggering conditions for hydro-morphological processes in different geomorphological settings in China. *International Journal of Applied Earth Observation and Geoinformation* **102**, 102350.

Wang, N., Lombardo, L., Tonini, M., Cheng, W., Guo, L. and Xiong, J. (2021c) Spatiotemporal clustering of flash floods in a changing climate (China, 1950–2015). *Natural Hazards and Earth System Sciences* **21**(7), 2109–2124.

Wang, Y. V. and Sebastian, A. (2022) Murphy Scale: A locational equivalent intensity scale for hazard events. *Risk Analysis* .

Wang, Z., Goetz, J. and Brenning, A. (2022b) Transfer learning for landslide susceptibility modelling using domain adaptation and case-based reasoning. *Geoscientific Model Development Discussions* pp. 1–30.

Xiao, C., Wu, P., Zhang, L. and Clark, R. T. (2018) Increasing flash floods in a drying climate over Southwest China. *Advances in Atmospheric Sciences* **35**(8), 1094–1099.

Xiong, J., Li, J., Cheng, W., Wang, N. and Guo, L. (2019) A GIS-based support vector machine model for flash flood vulnerability assessment and mapping in China. *ISPRS International Journal of Geo-Information* **8**(7), 297.

Xiong, J., Pang, Q., Cheng, W., Wang, N. and Yong, Z. (2020) Reservoir risk modelling using a hybrid approach based on the feature selection technique and ensemble methods. *Geocarto International* pp. 1–22.

671 Zhao, M., Cheng, C., Zhou, Y., Li, X., Shen, S. and Song, C. (2022) A global dataset
672 of annual urban extents (1992–2020) from harmonized nighttime lights. *Earth System*
673 *Science Data* **14**(2), 517–534.

674 Zielinski, P. (2017) Societal risk-how we measure and evaluate it. In *Proc. ICOLD 85th*
675 *Annual Meeting, Knowledge Based Dam Engineering Symposium. July*, pp. 3–7.